Hollow Au Nanosphere-Cu_2O Core-Shell Nanostructures with Controllable Core Surface Morphology

Yi-Hsuan Chiu[1,2,†], Sarah A. Lindley[2,3,†], Chun-Wen Tsao[1], Ming-Yu Kuo[1], Jason K. Cooper[3], Yung-Jung Hsu[1,4,], Jin Z. Zhang[2,*]*

[1] *Department of Materials Science and Engineering, National Chiao Tung University, Hsinchu 30010, Taiwan*

[2] *Department of Chemistry and Biochemistry, University of California, Santa Cruz, California 95064, United States*

[3] *Chemical Sciences Division, Lawrence Berkeley National Laboratory, Berkeley, California 94720, United States*

[4] *Center for Emergent Functional Matter Science, National Chiao Tung University, Hsinchu 30010, Taiwan*

Abstract

Design of metal-semiconductor interfaces and heterostructures is of strong interest for various catalytic applications including photocatalysis. In this work, a series of hollow Au nanosphere (HGN)-Cu_2O core-shell nanostructures with varying core surface rugosity are synthesized and investigated for possible photocatalytic applications. HGN surface rugosity is tuned by pH modification during galvanic exchange and carboxyl groups are utilized as coordination sites to deposit uniform Cu_2O shells onto the gold surfaces. Final core-shell structures are verified by transmission electron microscopy (TEM), scanning electron microscopy (SEM), energy dispersive X-ray spectrometry (EDS), and X-ray diffraction (XRD). Information regarding chemical state and electronic band structure is acquired by X-ray photoelectron spectroscopy (XPS) and ultraviolet photoelectron spectroscopy (UPS). Ultrafast transient absorption (TA) reveals that charge separation in bHGN-Cu_2O may effectively provide longer-lived photoexcited carriers, offering great potential for utilization in advanced photocatalytic processes.

1. Introduction

Metal-semiconductor core-shell nanostructures have attracted considerable attention because of their unique properties and functionalities from synergistic interaction between the two constituent components. Due to the ease of synthesis of metal-Cu_2O core-shell nanostructures, much effort has been devoted to exploring different core metals, such as Au, Ag, and Pd, as well as selectively tuning the resultant geometric parameters, such as size of the metal core, thickness, morphology and porosity of the Cu_2O shell.[1-3] Au nanoparticles (Au NPs) are particularly attractive cores due to their highly tunable optical and electronic properties.[4,5]

Hollow metal nanostructures offer many advantages over their solid metal counterparts, including higher surface-area-to-volume ratio for increased density of active sites and enhanced plasmonic performance in catalytic application.[6] In the case of Au-Cu_2O core-shell structures, hollow Au nanosphere (HGN)-Cu_2O have been shown to outperform Au NP-Cu_2O in the photodegradation of methyl orange under visible light irradiation, attributed to the Schottky barrier and plasmon-induced resonant energy transfer between the core and shell material.[7] The synthesis of HGNs is well controlled with respect to diameter, shell thickness, and uniformity[8] and the surface morphology of the HGN is also easily controllable through pH modification during galvanic exchange.[9] The effect of core surface morphology on the performance of core-shell materials for photocatalysis has not yet been investigated. An increase in surface rugosity may further increase the number of catalytic sites for additional activity enhancements. Photoactivation may also be advantageous in these systems. Cu_2O is considered to be a promising visible-light-driven photocatalyst due to its narrow bandgap, favorable band position, and high absorption coefficient.[10] Au is capable of functioning as a charge separation enhancer to improve overall carrier utilization.[11] The synergistic effect of Au and Cu_2O can be coupled with photoactivation for the development of highly efficient photocatalysts, and control of the core surface rugosity may be used to maximize the interfacial area.

Herein, we report the synthesis and characterization of bumpy HGN (bHGN)-Cu_2O core-shell nanostructures. To study the effect of core surface morphology, we control the HGN surface from smooth to very bumpy while maintaining a constant inner cavity diameter. The chemical state and electronic band structure of the samples are inspected with X-ray photoelectron spectroscopy (XPS) and ultraviolet photoelectron spectroscopy (UPS). The charge carrier relaxation and separation between the HGN core and Cu_2O shell materials are examined by ultrafast transient absorption (TA) spectroscopy. Combining these results, a plausible interfacial charge transfer mechanism for HGN-Cu_2O is proposed.

2. Experimental Section

2.1 Synthesis of solid Au NPs and HGNs

Solid Au NPs were synthesized using the well-known citrate-reduction method[12] in which $Na_3C_6H_5O_7$ (35.0 μL, 0.50 M) was injected into $HAuCl_4$ aqueous solution (100.0 mL, 0.25 mM) at 100 $°C$ under stirring for 20 minutes.

HGNs were prepared through galvanic exchange with sacrificial Co_xB_y NP templates, according to a previous report.[8] First, a 100 mL solution of 0.40 mM $CoCl_2$ and 4.0 mM $Na_3C_6H_5O_7$ was deaerated by bubbling with nitrogen for 1 hour. Then, 150.0 μL of 1.0 M fresh $NaBH_4$ reducing agent and 200.0 μL of 1.0 M aged $NaBH_4$ growth agent (1.0 M $NaBH_4$ which had hydrolyzed under ambient condition for 48 hours) were quickly mixed and injected into the deaerated cobalt salt solution. The solution turned brown/gray, indicating the reduction of Co^{2+} ions and the formation of the Co_xB_y scaffold. The solution was stirred for two minutes and then left to sit under nitrogen protection for an hour to allow full hydrolysis of $NaBH_4$. For galvanic exchange, 15.0 mL of the Co_xB_y NP solution was transferred to aqueous $HAuCl_4$ (15.0 mL, 53.3 μM) which was deaerated by bubbling with nitrogen for 1 hour in advance. The transfer was done in an air-free manner with a cannula under nitrogen protection. Due to the higher reduction potential of $AuCl_4^-$/Au (E_0 = +1.00 V vs standard hydrogen electrode (SHE)) than that of Co^{2+}/Co (E_0 = −¿0.28 V vs SHE),[13] galvanic exchange results in the formation of an intermediate Co_xB_y-Au core-shell structure. The resultant Co_xB_y-Au core-shell particles were stirred for

3 minutes before exposing to ambient conditions for oxidation of the residual Co_xB_y cores and formation of solvent-filled smooth HGNs (denoted as sHGNs). To control surface morphology, the galvanic exchange step was altered with respect to dissolved oxygen content and pH, according to a previous report.[8] To form slightly bumpy HGNs (shells with a small amount of nanoscaled protrusions, denoted as sbHGNs), galvanic exchange was carried out under ambient conditions (the $HAuCl_4$ solution was not deaerated and was open to ambient conditions during the Co_xB_y transfer). 15.0 mL of the Co_xB_y NP solution was transferred to aqueous $HAuCl_4$ (15.0 mL, 160.0 μM). To form bumpy HGNs (denoted as bHGNs), galvanic exchange was carried out under ambient conditions and the pH of the $HAuCl_4$ solution was increased to pH 4.0 with 1.0 M NaOH before galvanic exchange. Resultant HGNs were washed with deionized water, resuspended in 3 mM aqueous $Na_3C_6H_5O_7$ to fix the absorbance of HGN to be around 1.3 optical density (O.D.) for sHGN and sbHGN and 0.6 O.D. for bHGN, and stored in the refrigerator for later use.

2.2 Synthesis of Au-Cu_2O core-shell nanostructures

The growth of Cu_2O shell is conducted with a chemical reduction method using citrate ligands as the coordination reagent.[3] A 4.0 mL aliquot of citrate-protected Au NP or HGN colloids was dispersed in aqueous $CuSO_4$ (50.0 mL, 0.6 mM) at 35 °C, followed by simultaneous addition of NaOH (4.0 mL, 0.1 M) and *L*-ascorbic acid (LAA, 2.0 mL, 0.1 M) reduction agent. As the Cu_2O was deposited onto the Au surfaces, the reaction solution became yellow-green in color. Resultant products were washed with deionized water and ethanol for later use. For comparison purposes, pure Cu_2O nanostructures were synthesized by adding NaOH (2.4 mL, 0.1 M) and polyvinylpyrrolidone (PVP, 0.2 g, M_W=29,000 Da) to aqueous $CuSO_4$ solution (24.0 mL, 0.01 M), generating blue $Cu(OH)_2$ precipitate. Then, LAA (2.4 mL, 0.1 M) was added to the dispersion and stirred for 5 minutes. The resulting precipitates were orange-yellow in color and were also washed thoroughly with deionized water and ethanol.

2.3 Optical and Structural Characterization

Optical extinction spectra were recorded on an Agilent Cary 60 UV-Vis spectrophotometer. Scanning electron microscopy (SEM) with an energy dispersive spectrometer (EDS) was performed on an FEI Quanta 3D field emission microscope operated at 5.00 kV. The structural dimensions and surface morphology of the products were examined with a high-resolution transmission electron microscope (HR-TEM, JEOL, JEM-ARM200FTH) operated at 200 kV. The crystallographic structure and elemental analysis were investigated by X-ray diffraction (XRD, Bruker, D2 phaser) and EDS equipped on the TEM. The XPS data were collected on an ESCALAB Xi^+ (Thermo Fisher Scientific) using Al Kα radiation. All of the binding energies were calibrated by Pt 4 $f_{7/2}$ peak at 71.2 eV. The band structure of Au-Cu_2O was examined with UPS. The excitation source was He I ($h\upsilon$=21.22 eV) and a negative bias of −5 V was applied during the measurement.

2.4 Ultrafast TA and Photothermal Deflection Spectroscopy

Femtosecond TA measurements were performed using a Coherent Libra (Coherent, CA, USA) laser with pulse width of 100 fs and repetition rate of 1 kHz. The 800 nm output beam was split between a Coherent OPerA Solo optical parametric amplifier to generate a tunable pump beam and a CaF_2 crystal to generate a super-continuum white light probe. A wavelength of 400 nm was chosen for the pump beam and the pulse energy was tuned to 400 nJ using a neutral density filter. The pump beam was overlapped with the probe beam spatially and temporally at the sample. A motor-controlled translation stage was used to create a time delay interval of 0-500 ps or 0-10 μs between the pump and probe pulses. Differential transmission was detected over a ~400-800 nm spectral range using an Ultrafast Systems (Sarasota, FL, USA) TA measurement system, including a fiber-coupled grating spectrometer with Si complementary metal-oxide semiconductor detector arrays. All samples were prepared as thin films deposited on glass substrate.

Photothermal deflection spectroscopy (PDS) was performed on a home-built system consisting of a monochromatic laser-stimulated light source (EQ-77, Enertiq) for sample excitation and a stabilized HeNe laser probe. The excitation light was modulated with an optical shutter and the probe beam was amplified

and filtered with a current pre-amplifier. Probe signal was recorded with a lock-in amplifier. The film samples were immersed in perfluorohexane during measurement.

3. Results and Discussion

3.1 Structural and optical properties

TEM and SEM images for the Au particles are shown in Figure 1 (a). The diameters of solid Au NPs, sHGN, sbHGN, and bHGN were estimated to be 58 ±7, 52 ±7, 56±9, and 70 ±10 nm, respectively. As expected, the diameter of the HGN increases as the surface is made more rugose. The diameter of the inner cavity was measured to be 40±6, 42 ±7, and 41±7 nm for sHGN, sbHGN, and bHGN, respectively. The inner diameter is indeed expected to be similar for all HGNs reported herein as they were synthesized from the same cobalt-based sacrificial template.

The SEM images highlight the morphological differences among the various cores. The Au NPs are round and oblong with smooth surfaces.[6] The sHGN are highly spherical and smooth shells, as expected from anaerobic galvanic exchange. Under air-free conditions, galvanic exchange is able to occur in absence of any oxidation of cobalt in air, resulting in the formation of a smooth shell surface. The sbHGN have small protrusions on the shells, which are promoted under aerobic galvanic exchange and increased Au volume. Under aerobic conditions, oxidation of the Co_xB_y cores in air may disturb the process of galvanic exchange, resulting in an Au shell with nanoscaled protrusions.[6] The bHGN are highly rugose due to the addition of pH-modified galvanic exchange.[7] These results demonstrate the high morphological tunability of HGN via control of reaction conditions, particularly dissolved oxygen and pH, which is beneficial to study the effect of metal-semiconductor interfaces and heterostructures on catalytic activity. The resultant series of Au particles are used as scaffolds for the growth of Au-Cu_2O core-shell nanostructures.

Figure 1(b) shows an SEM image of pure Cu_2O (solid black border) as well as the corresponding core-shell structures after Cu_2O deposition onto the Au cores (solid colored borders). Overall diameters were determined to be 230±60 nm for pure Cu_2O and 160±10, 149±9, 180±10, and 190±20 nm for Au NP-

Cu_2O, sHGN-Cu_2O, sbHGN-Cu_2O, and bHGN-Cu_2O, respectively. For each core-shell structure, the Cu_2O shell is ~50-60 nm thick. It should be noted that pure Cu_2O has round, globular features. This is likely due to the PVP surfactant used in synthesis which favors formation of spherical instead of cubic nanostructures.[14] PVP is not required in the core-shell synthesis as the Au core provides a spherical template for deposition. As a result, due to directed deposition in absence of PVP, Cu_2O morphology in the core-shell structures is less globular and more angular. Interestingly, as the HGN surface morphology is taken from smooth to bumpy, the morphology of the Cu_2O shell also changes, becoming noticeably more faceted with increase in HGN rugosity. This was an unexpected result, and potentially beneficial, as the catalytic properties of Cu_2O have been shown to be highly dependent upon geometry and facet expression.[15] Since the core-shell interfacial area is greatly increased in the case of bHGN-Cu_2O, the catalytic performance of bHGN-Cu_2O is expected to be superior to that of Au NP-Cu_2O. Figure S1 (supporting information) further highlights the surface morphology of the different HGN cores and the corresponding core-shell nanostructures. The microstructural feature of the ensemble of core-shell nanostructures is also highly relevant to catalytic performance. Structural porosity and junctions between the constituent particles play important roles in catalytic reactions. Especially for those immobilized on supporting substrates, high porosity and rigid junctions can accelerate molecular migration and increase the number of active sites, both of which are favorable for heterogeneous catalytic reactions.

Extinction spectra for pure Cu_2O, the four different Au colloids, and the final core-shell nanostructures are displayed in Figure 1(c) alongside their corresponding EM images. Pure Cu_2O displays a broad extinction band around 500 nm, as is typical of the material and size.[3] Solid Au NPs show a surface plasmon resonance (SPR) band centered at 550 nm. Upon shell deposition, the SPR band red-shifts to ~700 nm due to the increase in refractive index from water ($n = 1.33$) to Cu_2O ($n = 2.5$-2.7).[16] The absorption feature ranging from 300-700 nm is attributed to the bandgap of the Cu_2O shell,[17] which corresponds well with the absorption feature of pure Cu_2O. For the HGNs, a narrow and symmetric SPR band was found at 630 nm for sHGN while a broader SPR band

was observed at 620 nm and 650 nm for the sbHGNs and bHGNs, respectively. Broadening of the SPR for bumpy particles is expected due to the roughening of the surface and formation of nanoscaled protrusions.[7,8] Upon deposition of the Cu_2O shell, the HGN SPR bands red-shift past 900 nm, again due to an increase in refractive index surrounding the cores. As the HGN cores become more rugose, the Cu_2O-related features in the visible region become multipeaked line shapes and slight red-shifts are observed. Similar spectral changes have been previously reported and are due to geometry- and facet-dependent optical features of Cu_2O.[17]

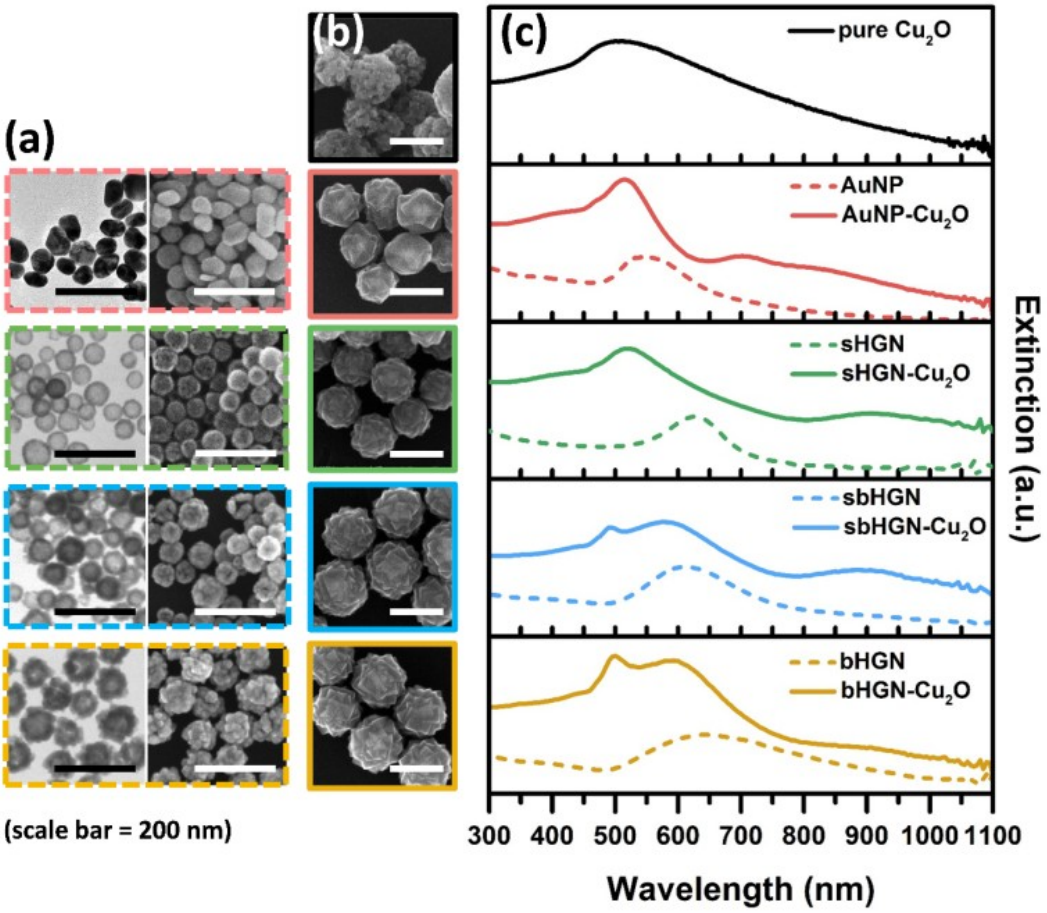

Figure 1. (a) TEM and SEM images for pure Cu_2O, Au NP, sHGN, sbHGN, and bHGN cores, with (b) SEM images of the corresponding core-shell nanostructures after Cu_2O deposition. (c) UV-visible extinction spectra are provided for each structure.

Microstructural analysis including TEM, HRTEM, and TEM-EDS supports the classification of Au core and Cu_2O shell, the uniformity in synthesis, and the preservation of the various core morphologies within the final core-shell structures. Figure S2(a) (supporting information) first shows the TEM image of Au-Cu_2O particles with high structural yield, demonstrating the advantage of the citrate-coordinating approach to the growth of core-shell nanostructures. As shown in the HRTEM images in Figure 2, the HGN-Cu_2O particles are highly uniform, with well-defined core and shell regions. The HGN cores are clearly visible, with rugosity still intact, suggesting that shell deposition does not disrupt the surface morphology of the cores. The successful formation of Cu_2O shells indicates that carboxylation of the HGN surface with trisodium citrate produced uniform coordination sites for Cu_2O deposition, regardless of HGN morphology. The d-spacing of 0.21 nm and 0.24 nm corresponds to the (200) planes of Cu_2O and (111) planes of Au, respectively, indicating heterogeneous nucleation of Cu_2O onto the HGN surface. For the bHGN-Cu_2O, the (200) planes of Au and (111) planes of Cu_2O are evident. EDS-mapping analysis clearly displays the presence of Au, Cu, and O elements. For each particle, Au signals were mainly confined to the central region while the Cu and O elements were evenly distributed over the whole structure, as expected in core-shell formation. XRD patterns indicate that the core-shell nanostructures are composed of *fcc* Au and cubic Cu_2O in absence of CuO or other Cu-based impurities, as displayed in Figure S2(b) (supporting information). Note that the area ratios of (111) and (200) peaks are respectively 1.05, 0.96, and 0.96 for sHGN-Cu_2O, sbHGN-Cu_2O, and bHGN-Cu_2O, revealing that the Cu_2O is isotropically grown onto the Au core surface.

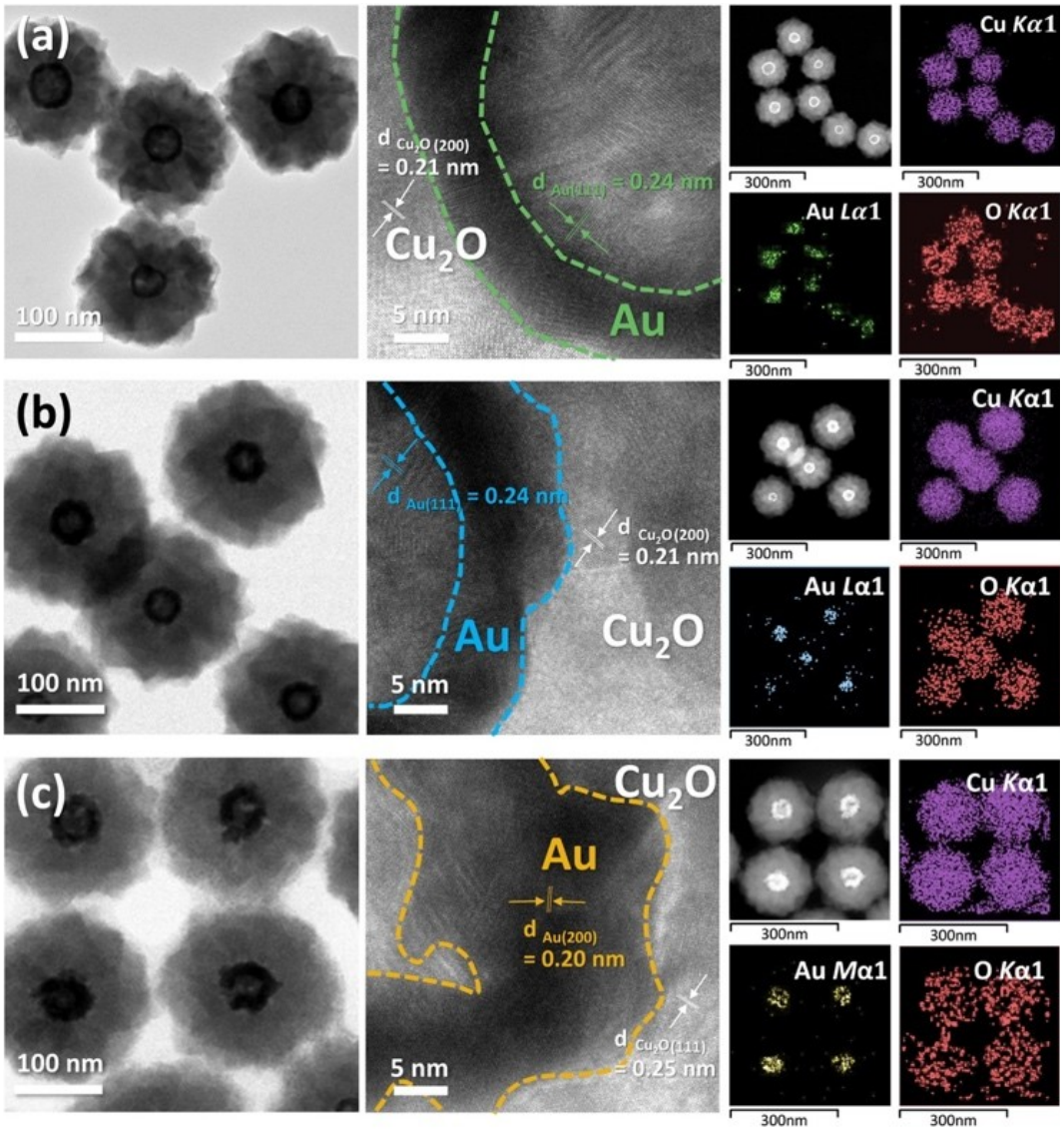

Figure 2. Microstructural analysis for (a) sHGN-Cu_2O, (b) sbHGN-Cu_2O, and (c) bHGN-Cu_2O core-shell nanostructures. Low and high magnification TEM images are provided with corresponding EDS-mapping.

3.2 Electronic band structure

The electronic band structures of pure Cu_2O and pure Au were measured with UPS in order to estimate the overall band structure of the core-shell system. In Figure 3(a)-(c), the photoemission spectra were corrected to zero as Fermi level (E_F), which revealed the typical secondary-electron cut-off energy at 16.63 eV and 16.43 eV for Cu_2O and Au. The work function, taken as the difference between the photon energy (21.22 eV) and cut-off energy, was

determined to be -4.59 eV and -4.79 eV for Cu_2O and Au, respectively. Spectral distribution close to the Fermi level represents the valence band structure of the test sample. Further linear extrapolation along the tangent of the spectrum onset reveals the valence band maximum with respect to the Fermi level (E_{VB}-E_F) is -0.69 eV for Cu_2O. The valence band maximum of Cu_2O was then determined to be -5.28 eV vs. vacuum. Moreover, the optical bandgap of Cu_2O was measured by using a Tauc plot, as shown in Figure 3(d), giving an apparent bandgap value of 2.22 eV. The conduction band minimum (E_{CB}) was then obtained by subtracting the optical bandgap value from the valence band maximum, which amounted to -3.06 eV vs. vacuum for Cu_2O.

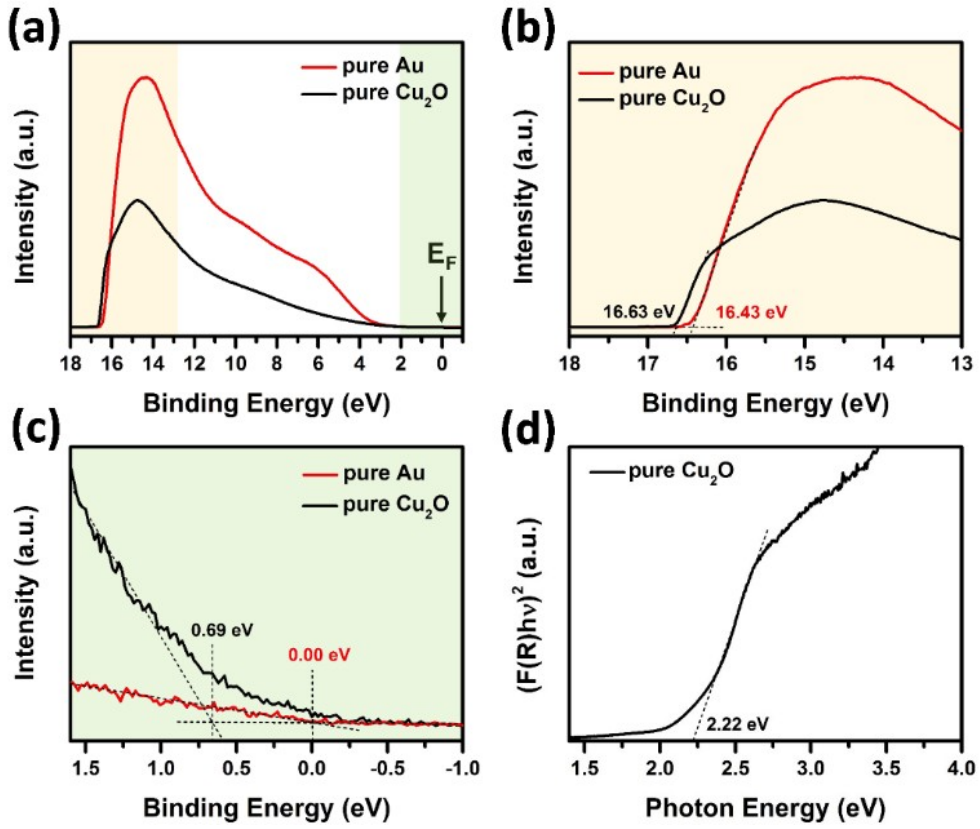

Figure 3. UPS spectra recorded on pure Au and pure Cu_2O at (a) secondary-electron cut-off region, (b) valence band distribution region. (c) display the valence band maximum onset for Au and Cu_2O. (d) shows the Tauc plot of pure Cu_2O for determining bandgap.

3.3 Charge carrier dynamics

To characterize charge carrier dynamics for HGN-Cu_2O core-shell structures, TA spectroscopy was performed on pure Cu_2O, sHGN-Cu_2O, and bHGN-Cu_2O films. Transient difference transmission (dT) was recorded following photoexcitation with a 400 nm pump and interrogation with a white light continuum probe (425-775 nm) over a time delay range of 0-200 ps and 0-10 μs between the pump and probe pulses. 400 nm was chosen for above-band edge excitation of Cu_2O but also excites the sHGN and bHGN via the interband transition of Au. Resultant dT spectra at 100 ns delay are shown in Figure 4(a). All samples show a sharp transient bleach (TB) feature at 490 nm which can be assigned to Cu_2O. The sHGN-Cu_2O and bHGN-Cu_2O structures show an additional TB centered at 550 nm.

PDS spectra are displayed in Figure 4(b). As PDS signal is generated from a photothermal effect, it represents the absorption component of extinction. The absorption feature from 400-500 nm is consistent for all samples and corresponds well with the band edge of Cu_2O. The NIR absorption features centered at ~900 nm for the HGN-Cu_2O samples arise from the red-shifted SPR band of the HGN cores. A new feature at 550 nm appears for the core-shell samples, which lies in between the spectral features of Cu_2O and HGN. It has been shown experimentally and theoretically that the absorption features of Cu_2O are size and morphology dependent, manifesting multiple peaks across the visible.[17] This new feature may be the result of strain and/or defect absorption tailing arising from the growth of Cu_2O. Depositing Cu_2O around the surface of spherical HGN particles likely causes strain in the Cu_2O as it attempts to conform to the surface during growth. Strain is known to cause changes in electronic structure similar to defect absorption tailing. This effect is heightened when the surface of the HGN is highly roughened, which should cause more strain in the Cu_2O shell, increasing the corresponding signal at 550 nm in the PDS spectrum for bHGN-Cu_2O. The absorption assignment being related to Cu_2O will be addressed in additional detail with the transient spectral response.

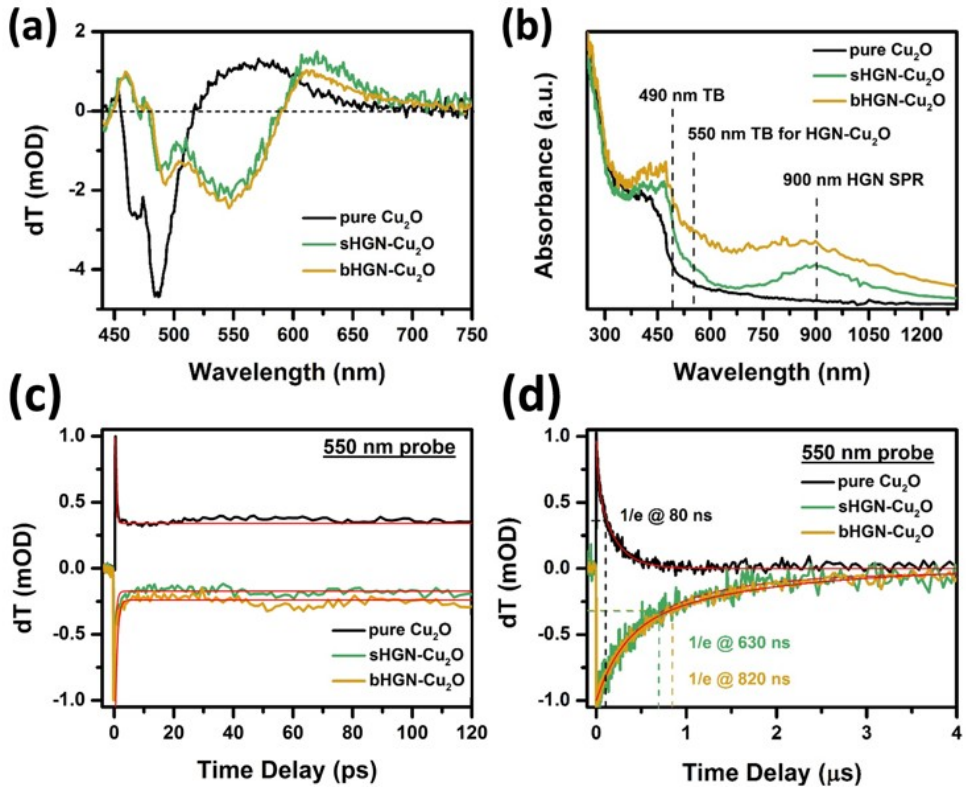

Figure 4. (a) TA spectral profile after 400 nm excitation and (b) PDS spectra for Cu_2O, sHGN-Cu_2O, and bHGN-Cu_2O nanostructures. Charge carrier decay dynamics are shown for 550 nm probe on the (c) ultrafast (0-120ps) and (d) longer (0-4 μs) timescales.

Charge carrier recombination dynamics were investigated for Cu_2O, sHGN-Cu_2O, and bHGN-Cu_2O samples at 490 nm (to probe Cu_2O) and 550 nm (to probe the mixed signal). As displayed in Figure S3(a) (supporting information), all samples show similar ultrafast decay profiles at 490 nm, with the majority of the TB signals recovering within a few ps. Thus, charge carrier dynamics are not appreciably different between the samples when Cu_2O is excited and probed. The corresponding longer time dynamics are shown in Figure S3(b) (supporting information). The recoveries are again very similar, with samples showing nearly complete decay within 10 μs. Corresponding fit values for the 490 nm probe are tabulated in Table S1 (supporting information). For the 550 nm probe, the samples again show rapid charge carrier recombination, with more than half of the signal decaying within the first few ps, as displayed in Figure 4(c). The rapid decay is followed by a persistent offset throughout the 120 ps time window shown. The data were fit to a single exponential, which revealed lifetimes of 0.34 ± 0.02 ps, 0.51 ± 0.03 ps, and 0.49 ± 0.04 ps, with y-

offsets of 0.34, 0.17, and 0.24, for Cu_2O, sHGN-Cu_2O, and bHGN-Cu_2O, respectively. Thus, for the HGN-Cu_2O samples, a smaller percentage of carriers persist throughout the 500 ps window, suggesting faster decay on the ultrafast timescale. Interestingly, the opposite trend occurs on the longer timescale. Figure 4(d) shows the transient profiles for the 0-4 μs time window. The data were fit to a double exponential, which revealed lifetimes of 0.02 ± 0.01 and 0.15 ± 0.01 μs for Cu_2O, 0.35 ± 0.07 and 1.1 ± 0.2 μs for sHGN-Cu_2O, and 0.25 ± 0.09 and 1.2 ± 0.2 μs for bHGN-Cu_2O. All fit values for the 550 nm probe are tabulated in Table S2 (supporting information). The incorporation of the HGN core significantly increases the charge carrier lifetime in the core-shell nanostructures for the mixed-signal probe region. This may be most simply shown with 1/e decay times. The 1/e decay time of 80 ns for Cu_2O is lengthened to 630 ns for sHGN-Cu_2O. The 1/e decay time is then further lengthened to 820 ns for bHGN-Cu_2O. This additional increase in lifetime was attributed to improved charge transfer at the Au/Cu_2O interface in the case of the bHGN core.

It should be noted that the faster decay of bHGN-Cu_2O on the ultrafast timescale but slower decay on the longer timescale (in comparison to pure Cu_2O) may be due to the difference between HGN- and Cu_2O-related lifetimes; for the bHGN-Cu_2O sample, there may be more Au character in the ultrafast data than the longer lifetime data. To support this assertion, the films were excited with 400 nm and probed in the NIR to gauge the lifetime of HGN-related charge carriers. Figure S4 and S5 (supporting information) show dA signal for 9 probe wavelengths ranging from 900-1600 nm over the course of a 0-2750 ps time delay for Cu_2O and bHGN-Cu_2O films. Since 400 nm excites both core and shell components, the resultant bHGN-Cu_2O signals are a mixture of a strong bHGN-related bleach feature and a Cu_2O-related absorption feature. The bleach dominates the signal at 900 nm and becomes less prominent at longer wavelengths, nearly disappearing at 1650 nm, as expected from the location and breadth of the bHGN SPR. The bleach is short-lived, recovering within 5 ps and transitioning to a low-amplitude absorption which follows that of Cu_2O and nearly fully decays within the 2750 ps time window. This absorption feature has been noted in similar metal oxide films and attributed to

thermal effects.[18,19] These results suggest that short-lived HGN-related charge carriers are not responsible for the long-lived bleach at 550 nm. We conclude that HGN contribution to the 550 nm transient signal is relatively low and the signal is mostly Cu_2O in nature, particularly on the longer time scales. Structural changes within the Cu_2O material itself (including an increase in overall particle diameter, an increase in angularity of the surface features, and potential increase in bandgap defect states) may be responsible for the heightened absorption around 550 nm upon incorporation of the Au core. Rigorous modeling of the Cu_2O and HGN-Cu_2O extinction and band structures, which is beyond the scope of the current work, is needed to fully confirm the identity of this feature.

Based on the above results and the UPS data, we create the band structure for HGN-Cu_2O and propose the following mechanism for interfacial charge transfer under light illumination, as shown in Figure 5. For HGN-Cu_2O, a typical metal-semiconductor band alignment was considered. Under light illumination, the HGN core can function as charge separation enhancer by accepting photoexcited electrons from Cu_2O, therefore promoting the carrier utilization efficiency. On the other hand, the combination of HGN and Cu_2O could result in modified energy levels at the HGN/Cu_2O interface, producing long-lived carriers to enhance the efficiency of carrier utilization. As a result of the interfacial electron transfer, more photoexcited carriers may be available for catalytic reactions. Note that the E_{CB} and E_{VB} of Cu_2O was -3.06 and -5.28 eV vs. vacuum, corresponding to -1.44 and +0.78 V vs. NHE, respectively. Although the photoexcited holes of Cu_2O are unable to decompose H_2O into O_2 ($E_{H2O/O2}$ = +1.23 V vs. NHE), the photoexcited electrons in Cu_2O may transfer to HGN and further reduce O_2 to form $\cdot O_2^-$ radicals ($E_{O2/\cdot O2-}$ = +0.11 V vs. NEH),[20] an important type of radical that can catalyze various advanced oxidation processes. In addition, the photoexcited holes of Cu_2O are also highly reactive, which can participate in bacterial disinfection for environmental purification applications.[3] The heterojunction is therefore important in photoactivated catalysis. Several literature reports have revealed chemical instability of Cu_2O nanostructures, especially when light irradiation is

applied.[21,22] However, with appropriate surface modification, the samples can still exhibit satisfactory performance under long-term operation.[23,24]

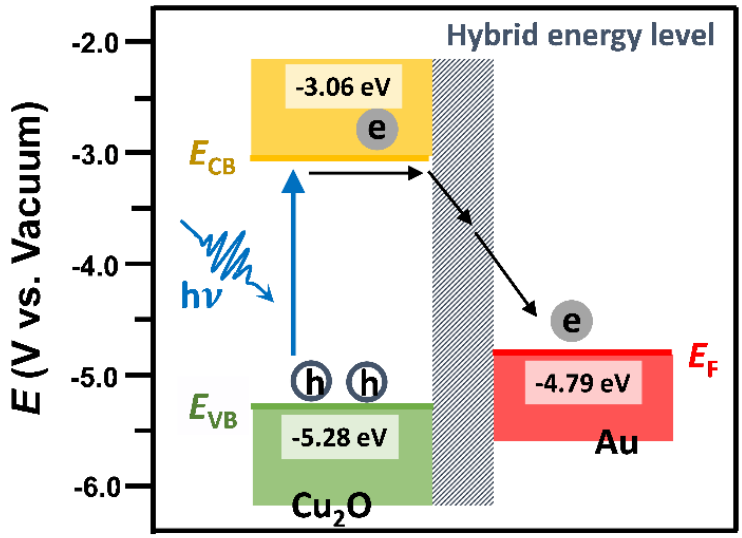

Figure 5. Energy band diagram and mechanism of interfacial charge transfer for HGN-Cu_2O.

Conclusions

A series of Au-Cu_2O core-shell nanostructures have been synthesized by varying the structure of the Au core to study the influence of core morphology on the optical and interfacial charge transfer dynamics. TA data suggest longer-lived charge carriers in the case of bHGN-Cu_2O, allowing the photoexcited carriers to be efficiently utilized in photocatalytic reactions. On this basis, a band diagram was constructed to illustrate interfacial charge separation. This work illustrates the importance of engineering nanostructured interfaces in the rational design of high-performance core-shell photocatalysts.

Associate Content

Supporting Information

SEM image, XRD patterns, transient absorption spectra, fitting parameters of the samples. This material is available free of charge via the Internet at http://pubs.acs.org.

Author Information

Corresponding Author

*E-mail: zhang@ucsc.edu (J. Z. Zhang)

*E-mail: yhsu@cc.nctu.edu.tw (Y.-J. Hsu)

† These authors contributed equally to this work.

Notes

The authors declare no competing financial interest.

Acknowledgements

This work was financially supported by the Ministry of Science and Technology (MOST) of Taiwan under grants MOST 107-2113-M-009-004, MOST 108-2628-M-009-004-MY3 and MOST 108-2218-E-009-039-MY3. We also thank Delta Dental Health Associates, Smart Technologies, and NASA through the Merced Nanomaterials Center for Energy and Sensing (MACES) for support. We acknowledge T. Yuzvinsky for SEM and the W.M. Keck Center for Nanoscale Optofluidics for use of the FEI Quanta 3D dual beam microscope. We also acknowledge the contribution from the Joint Center for Artificial Photosynthesis, a DOE Energy Innovation Hub, supported through the Office of Science of the U.S. Department of Energy under award no. DE-SC0004993. Y.-J. Hsu also acknowledges the budget support from the Center for Emergent Functional Matter Science of National Chiao Tung University from The Featured Areas Research Center Program within the framework of the Higher Education Sprout Project by the Ministry of Education in Taiwan.

References

1. Lin, Y.-K.; Chiang, Y.-J.; Hsu, Y.-J., Metal–Cu_2O core–shell nanocrystals for gas sensing applications: Effect of metal composition. *Sensor. Actuat. B: Chem.* **2014,** *204*, 190-196.

2. Yang, Y.-C.; Wang, H.-J.; Whang, J.; Huang, J.-S.; Lyu, L.-M.; Lin, P.-H.; Gwo, S.; Huang, M. H., Facet-dependent optical properties of polyhedral Au–Cu_2O core–shell nanocrystals. *Nanoscale* **2014,** *6*, 4316-4324.

3. Kuo, M.-Y.; Hsiao, C.-F.; Chiu, Y.-H.; Lai, T.-H.; Fang, M.-J.; Wu, J.-Y.; Chen, J.-W.; Wu, C.-L.; Wei, K.-H.; Lin, H.-C.; et al., Au@Cu_2O core@shell nanocrystals as dual-functional catalysts for sustainable environmental applications. *Appl. Cataly. B: Environ.* **2019,** *242*, 499-506.
4. Pu, Y.-C.; Wang, G.; Chang, K.-D.; Ling, Y.; Lin, Y.-K.; Fitzmorris, B. C.; Liu, C.-M.; Lu, X.; Tong, Y.; Zhang, J. Z.; et al., Au Nanostructure-Decorated TiO_2 Nanowires Exhibiting Photoactivity Across Entire UV−visible Region for Photoelectrochemical Water Splitting. *Nano Lett.* **2013**, *13*, 3817-3823.
5. Rej, S.; Hsia, C.-F.; Chen, T.-Y.; Lin, F.-C.; Huang, J.-S.; Huang, M. H., Facet-dependent and light-assisted efficient hydrogen evolution from ammonia borane using gold–palladium core–shell nanocatalysts. *Angew.Chem. Int. Ed.* **2016**, *55*, 7222-7226.
6. Genç, A.; Patarroyo, J.; Sancho-Parramon, J.; Bastús, N.; Puntes, V.; Arbiol, J., Hollow metal nanostructures for enhanced plasmonics: synthesis, local plasmonic properties and applications. *Nanophotonics* **2017**, *6*, 193-213.
7. Lu, B.; Liu, A.; Wu, H.; Shen, Q.; Zhao, T.; Wang, J., Hollow Au–Cu_2O core–shell nanoparticles with geometry-dependent optical properties as efficient plasmonic photocatalysts under visible light. *Langmuir* **2016,** *32*, 3085-3094.
8. Lindley, S. A.; Cooper, J. K.; Rojas-Andrade, M. D.; Fung, V.; Leahy, C. J.; Chen, S.; Zhang, J. Z., Highly tunable hollow gold nanospheres: gaining size control and uniform galvanic exchange of sacrificial cobalt boride scaffolds. *ACS Appl. Mater. Interfaces* **2018,** *10*, 12992-13001.
9. Lindley, S. A.; Zhang, J. Z., Bumpy hollow gold nanospheres for theranostic applications: effect of surface morphology on photothermal conversion efficiency. *ACS Appl. Nano Mater.* **2019,** *2*, 1072-1081.
10. Li, C.; Li, Y.; Delaunay, J.-J., A novel method to synthesize highly photoactive Cu_2O microcrystalline films for use in photoelectrochemical cells. *ACS Appl. Mater. Interfaces* **2014,** *6*, 480-486.
11. Han, N. S.; Kim, D.; Lee, J. W.; Kim, J.; Shim, H. S.; Lee, Y.; Lee, D.; Song, J. K., Unexpected size effect observed in ZnO-Au composite photocatalysts. *ACS Appl. Mater. Interfaces* **2016,** *8*, 1067-1072.
12. Ji, X.; Song, X.; Li, J.; Bai, Y.; Yang, W.; Peng, X., Size control of gold nanocrystals in citrate reduction: the third role of citrate. *J. Am. Chem. Soc.* **2007,** *129*, 13939-13948.
13. Lu, Y.; Zhao, Y.; Yu, L.; Dong, L.; Shi, C.; Hu, M.-J.; Xu, Y.-J.; Wen, L.-P.; Yu, S.-H., Hydrophilic Co@Au yolk/shell nanospheres: synthesis, assembly, and application to gene delivery. *Adv. Mater.* **2010,** *22*, 1407-1411.
14. Bi, J.; Wu, S.; Xia, H.; Li, L.; Zhang, S., Synthesis of monodisperse single-crystal Cu2O spheres and their application in generating structural colors. *J. Mater. Chem. C* **2019,** *7*, 4551-4558.
15. Huang, M. H.; Madasu, M., Facet-dependent and interfacial plane-related photocatalytic behaviors of semiconductor nanocrystals and heterostructures, *Nano Today* **2019**, *28*, 100768.
16. Rej, S.; Wang, H.-J.; Huang, M.-X.; Hsu, S.-C.; Tan, C.-S.; Lin, F.-C.; Huang, J.-S.; Huang, M. H., Facet-dependent optical properties of Pd–Cu_2O core–shell nanocubes and octahedra. *Nanoscale* **2015,** *7*, 11135-11141.

17. Zhang, L.; Blom, D. A.; Wang, H., Au–Cu_2O core–shell nanoparticles: a hybrid metal-semiconductor heteronanostructure with geometrically tunable optical properties. *Chem. Mater.* **2011,** *23*, 4587-4598.
18. Hayes, D.; Hadt, R. G.; Emery, J. D.; Cordones, A. A.; Martinson, A. B. F.; Shelby, M. L.; Fransted, K. A.; Dahlberg, P. D.; Hong, J.; Zhang, X.; et al., Electronic and nuclear contributions to time-resolved optical and X-ray absorption spectra of hematite and insights into photoelectrochemical performance. *Energy Environ. Sci.* **2016,** *9*, 3754-3769.
19. Cooper, J. K.; Reyes-Lillo, S. E.; Hess, L. H.; Jiang, C.-M.; Neaton, J. B.; Sharp, I. D., Physical origins of the transient absorption spectra and dynamics in thin-film semiconductors: the case of $BiVO_4$. *J. Phys. Chem. C* **2018,** *122*, 20642-20652.
20. Hirakawa, T.; Nosaka, Y., Properties of O_2•- and OH• formed in TiO_2 aqueous suspensions by photocatalytic reaction and the influence of H_2O_2 and some oons. *Langmuir* **2002**, *18*, 3247-3254.
21. Thoka, S.; Lee, A.-T.; Huang, M. H. Scalable synthesis of size-tunable small Cu_2O nanocubes and octahedra for facet-dependent optical characterization and pseudomorphic conversion to Cu nanocrystals, *ACS Sustainable Chem. Eng.* **2019**, *7*, 10467-10476.
22. Toe, C. Y.; Zheng, Z.; Wu, H.; Scott, J.; Amal, R.; Ng, Y. H. Photocorrosion of cuprous oxide in hydrogen production: rationalising self-oxidation or self-reduction, *Angew. Chem.* **2018**, *130*, 13801-13805.
23. Pan, L.; Liu, Y.; Yao, L.; Ren, D.; Sivula, K.; Grätzel, M.; Hagfeldt, A., Cu_2O photocathodes with band-tail states assisted hole transport for standalone solar water splitting. *Nat. Commun.* **2020**, *11*, 318.
24. Li, Y.; Zhong, X.; Luo, K.; Shao, Z. A hydrophobic polymer stabilized p-Cu_2O nanocrystal photocathode for highly efficient solar water splitting, *J. Mater. Chem. A* **2019**, *7*, 15593-15598.

TOC Graphic

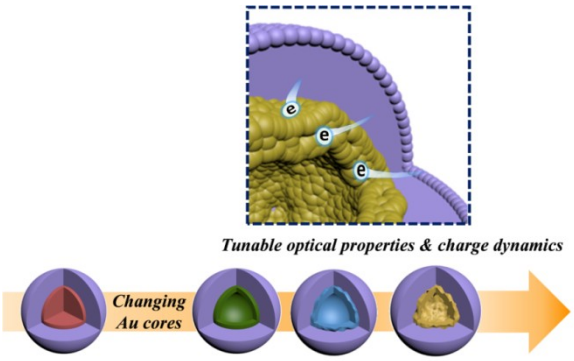
e
e
e
Tunable optical properties & charge dynamics
Changing
Au cores